Astronomy & Astrophysics manuscript no. paper110430
May 3, 2011

Effects of a low electron distribution cutoff on multiwavelength spectra and light curves of GRB afterglows

M. Petropoulou[1], A. Mastichiadis[1] & T. Piran[2]

[1] Department of Physics, University of Athens, Panepistimiopolis, GR 15783 Zografos, Greece
[2] The Racah Institute of Physics, The Hebrew University, Jerusalem, Israel

Received ... / Accepted ...

ABSTRACT

Aims. We investigate the behavior of the frequency-centered light curves expected within the standard model of Gamma Ray Bursts allowing the maximum electron energy ($\gamma_{\rm max}$) to be a free parameter permitted to take low values.
Methods. We solve the spatially averaged kinetic equations which describe the simultaneous evolution of particles and photons, obtaining the multi-wavelength spectra as a function of time. From these we construct the frequency-centered light curves giving emphasis in the X-ray and optical bands.
Results. We show that in cases where $\gamma_{\rm max}$ takes low values, the produced X-ray light curves show a plateau as the synchrotron component gives its place to the Synhro Self-Compton one in the X-ray band.

Key words. gamma-rays: theory – acceleration of particles – radiation mechanisms: non-thermal

1. Introduction

Gamma-Ray Bursts (GRBs) are attributed to a release of a very large amount of energy ($\sim 10^{51} - 10^{52}$ ergs) into a small region of space ($\lesssim 100$ km) over a short period of time ($\sim 10 - 10^2$ s for long GRBs and $\lesssim 2$ s for short GRBs). These energetic events have two characteristic radiative signatures: (i) the prompt γ-ray and (ii) the afterglow emission. The detection of high energy photons ($\epsilon_\gamma \gg 1$ MeV) implies sources of radiation moving at relativistic speeds with Lorentz factors Γ exceeding 100 (Fenimore et al. 1993; Lithwick & Sari 2001; Piran 1999).

While many issues concerning the prompt emission are still open, the afterglow, i.e. the lower energy long lasting emission, is believed to arise from the interaction of the relativistic ejecta with the ambient matter and can be adequately described by the so-called 'standard' model (Rees & Mészáros 1992; Paczynski & Rhoads 1993; Mészáros & Rees 1997). According to this, the relativistic blast wave produced from the explosion can energize the external medium, i.e. accelerate electrons (and possibly protons) to high energies and generate magnetic fields. The relativistic electrons radiate by synchrotron and inverse Compton radiation which is essentially the observed afterglow emission. However, in order to calculate the radiated photon spectra, one needs a detailed prescription of the electron distribution function and of the magnetic field. This is usually done by postulating that the electrons have a power law distribution between a minimum ($\gamma_{\rm min}$) and a maximum ($\gamma_{\rm max}$) cutoff with an overall energy density content which is a a fixed fraction (usually denoted by $\epsilon_{\rm e}$) of the total post-shock internal energy density U while an analogous argument can be made for the magnetic field energy which takes a fraction $\epsilon_{\rm B}$ of U. A significant amount of work has been performed by many researchers in calculating the multiwavelength spectra and light curves of GRB afterglows either based directly on the above prescription (Dermer & Chiang 1998; Sari et al. 1998; Panaitescu & Mészáros 1998; Wijers & Galama 1999; Dermer et al. 2000; Panaitescu & Kumar 2000; Granot & Sari 2002) or using different variations (Granot & Kumar 2006; Fan & Piran 2006; Panaitescu et al. 2006; Zhang et al. 2006; Nousek et al. 2006).

In the present paper we focus on the effects that a low $\gamma_{\rm max}$ will bring on the multiwavelength spectra and light curves of the afterglow emission. This has not been treated thus far as it is implicitly assumed that $\gamma_{\rm max}$ is very large and its radiative signature does not contribute to any observable band. However, if it has a low value, then a break might appear successively in various energy bands of diminishing energy as the synchrotron component gives gradually its position to the SSC one. This will produce light curves which are not any more pure power laws but have more complicated shapes.

The paper is structured as follows. Is §2 we describe the principles of the model and discuss, in a qualitative way, some of the results. In §3 we quantify the above and we derive some analytical relations between the initial parameters, which, when satisfied, will produce different types of X-ray light curves. In §4 we make a tentative connection of our results to observations. Finally in §5 we conclude and give a brief discussion of the basic points of the present work.

2. The Model

2.1. First principles

The general framework of the model we present here is based on the standard GRB afterglow model, al-

Send offprint requests to: A. Mastichiadis

beit with some modifications regarding mainly the approach to the physical problem (Fan et al. (2008); Petropoulou & Mastichiadis (2009) – henceforth PM09). For the sake of completeness we repeat here its basic premises: as the Relativistic Blast Wave (RBW) usually associated with GRB afterglows is expanding, it accelerates by some unspecified mechanism electrons of the circumstellar medium to high energies. These are assumed to be injected behind the shock front in a volume of radius R containing a tangled magnetic field B. The particles suffer radiative and adiabatic losses, evolving with radius. At the same time they emit radiation by synchrotron and inverse Compton radiation. Therefore, at each radius there is a coupling between electrons and photons, in the sense that the electron distribution function determines the photon spectrum and, at the same time, the photons determine the electron distribution function through inverse Compton losses and, possibly, pair reinjection. The usual procedure of approaching the problem is to solve simultaneously two coupled kinetic equations for the distribution functions of electrons and photons which, when solved, give the aforementioned quantities as functions of radius and energy. The most relevant physical processes which are included are: electron synchrotron radiation, synchrotron self absorption, inverse Compton scattering (both in the Thomson and Klein-Nishina regimes), photon-photon pair production and adiabatic losses (for a more detailed discussion regarding the physical processes see Mastichiadis & Kirk (1995); Pe'er & Waxman (2004)).

To obtain the multiwavelength (hereafter MW) spectrum of GRBs at each radius r of the relativistic blast wave one needs to specify the Lorentz factor of the flow $\Gamma(r)$, the comoving radius of the source $R = r/\Gamma$, the magnetic field strength $B(r)$ – determined indirectly through the parameter $\epsilon_{\rm B}$, and three parameters related to the electron injection, i.e. their total power – determined by the parameter $\epsilon_{\rm e}$, their slope p of the power law at injection and the maximum cutoff of their distribution $\gamma_{\rm max}$ – the minimum cutoff $\gamma_{\rm min}$ is defined in terms of the other parameters by equation (11).

2.2. Multiwavelength spectra

The approach described above allows one to calculate the photon MW spectra self-consistently while it inherently addresses questions about whether the electrons are in the fast or slow cooling regime. Moreover it can calculate the spectrum in various regimes without resorting in a piecewise succession of broken power laws which becomes problematic in cases where the characteristic frequencies are rather close to one another. Finally, it takes into account SSC losses which, as PM09 have shown – see also Sari & Esin (2001), can alter significantly the electron spectrum and therefore, the photon spectrum, even in the well-studied synchrotron regime.

Some of the above are exemplified in Fig. 1 which depicts a generic case of a MW spectrum in the case of a power-law electron injection with $\gamma_{\rm max}$ not much greater than $\gamma_{\rm min}$. As the parameters have been chosen so as the radiating electrons to be partly in the uncooled regime, the synchrotron component consists, at least in theory (Sari et al. 1998), of four segments: (1) synchrotron self-absorbed part below $\nu_{\rm ssa}$, (2) typical synchrotron low energy part for $\nu_{\rm ssa} < \nu < \nu_{\rm s,min}$, (3) uncooled part for $\nu_{\rm s,min} < \nu < \nu_{\rm s,c}$ and (4) cooled part for $\nu_{\rm s,c} < \nu < \nu_{\rm s,max}$. One could add here (5) the synchrotron exponential cutoff which appears above $\nu_{\rm s,max}$. Between these segments power laws of different slopes should appear, however due to the proximity of the lower and upper electron cutoffs, the turnovers in frequency have been smeared out and the spectrum appears to curve continuously without any clearly defined power-law regime, at least for frequencies above $\nu_{\rm s,min}$.

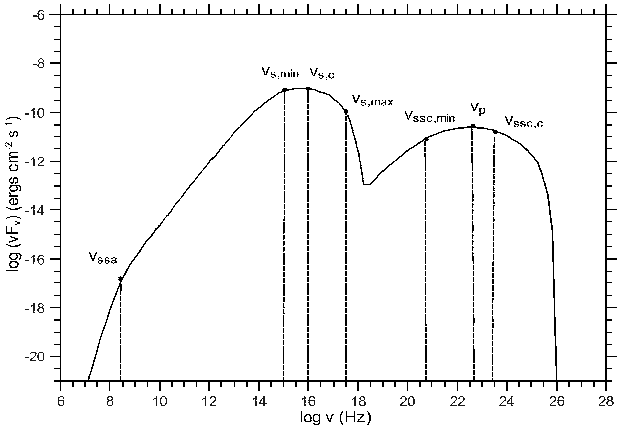

Fig. 1. Multiwavelength spectrum expected for a case where the upper electron cutoff is not much greater than the lower one – in the present case $\gamma_{\rm max} = 10^4$ and $\gamma_{\rm min,0} = 5.6\times10^3$. The complete set of the parameters used is: $E_0 = 10^{54}$ ergs, $\Gamma_0 = 400$, $n_0 = 1$ part/cm^3, $\epsilon_{\rm B} = 0.005$, $\epsilon_{\rm e} = 0.01$ and $p = 2.3$. Both synchrotron and SSC components of the spectrum appear to be continuously curved without any clear power law segments (at least for frequencies below $\nu_{\rm s,min}$ and $\nu_{\rm ssc,min}$ respectively) mainly due to the proximity of $\gamma_{\rm max}$ and $\gamma_{\rm min}$. The characteristic frequencies indicated in the figure are discussed in the text.

The same holds for the SSC component: this is much broader, as expected, than the synchrotron one and it also shows a continuous curvature. In Fig. 1 three characteristic frequencies of the SSC component are indicated: $\nu_{\rm ssc,min} = \frac{4}{3}\gamma_{\rm min}^2\nu_{\rm s,min}$, $\nu_{\rm ssc,c} = \frac{4}{3}\gamma_{\rm c}^2\nu_{\rm s,c}$ and the peak frequency $\nu_{\rm p}$. Sari & Esin (2001) have shown analytically that the peak frequency of the SSC component in the slow cooling regime is given by $\nu_{\rm ssc,c}$. However, this is not expected when a relatively low $\gamma_{\rm max}$ is taken into account, as in the case of Fig. 1. An analytic calculation (which can be found in detail in the Appendix) of the SSC peak frequency can also be done, in the case of an electron pure power law distribution, having limits between $\gamma_{\rm min}$ and $\gamma_{\rm max}$. The SSC peak frequency is then given by $\frac{4}{3}\gamma_{\rm max}^2\nu_{\rm s,min}$ which equals to 1.4×10^{23} Hz for the example given in Fig. 1. The numerically calculated peak frequency is however different: $\nu_{\rm p} = 4.4\times10^{22}$ Hz $\approx \frac{4}{3}\gamma_{\rm c}^2\nu_{\rm s,min}$. This simple example shows that the presence of the Compton logarithm (Gould 1979) combined with the fact that the electron distribution might have at least two breaks, one at $\gamma_{\rm min}$ and one at $\gamma_{\rm c}$, makes a simple analytic approach complicated. Nevertheless, for the specific example one can clearly see in νF_ν units a rising part, a broad peak and a declining part.

2.3. Light curves

Based on the above it is straightforward to construct light curves at various frequencies. However, it is worth describing qualitatively a case where cutoff effects in the synchrotron component appear due to a low value of $\gamma_{\rm max}$. Assume a certain observing window between two frequencies. Assume also that the initial parameters are such as initially the flux in this window to be dominated by the synchrotron component. As time evolves in the observer's frame, he/she will first observe the various parts of the synchrotron component passing through it, as first was suggested by Sari et al. (1998). Therefore at some point in time, which we will call $t_{\rm br,1}$, the combination of Γ, B and $\gamma_{\rm max}$ will be such that the flux in the observing window will be dominated by the exponential cutoff of the synchrotron component. This will result in a natural steepening of the light curve. In the hypothetical case where the SSC component is absent, the observer would have seen an ever increasing steepening of both the spectral index and of the light curve until the flux would drop to very low levels, below the sensitivity of any instrument. In reality, however, at some level the SSC component must appear in the observing window and start dominating the flux there. This would naturally result in a flattening of the light curve as the observer starts sampling photons not from the synchrotron but from the SSC component. Depending on the relation between $\gamma_{\rm min}$ and $\gamma_{\rm max}$, at time $t = t_{\rm br,1}$ the SSC component could be, broadly speaking, in any of its three spectral regimes (i.e. rising, peak or declining). As we elaborate in the next section, if the SSC component becomes dominant while still early in its rising part, the light curve will show a sharp turnover which will result in a shallow decline of the flux, i.e a plateau. If, on the other hand, the transition from the synchrotron to SSC occurs while the latter is close to the peak or during its declining part, the light curve will show a more gentle flattening.

Figures 2 and 3 present the results of a run showing an X-ray plateau. Figure 2 shows snapshots of the MW spectra at five different times, obtained for a GRB at $z = 1$ with $E_0 = 10^{54}$ ergs, $\Gamma_0 = 400$, $n_0 = 1$ part/cm^3, $\epsilon_{\rm B} = 0.001$, $\epsilon_{\rm e} = 0.025$, $p = 2.3$ and $\gamma_{\rm max} = 2.24 \times 10^4$. One can see that at early times the X-ray band is dominated by the tail of the synchrotron component which in about $t \sim 10^3$ s has given its position entirely to the SSC one. This trend is repeated once more at much later times ($t \gtrsim 5 \times 10^5$ s) in the optical band. Figure 3 shows the corresponding optical and X-ray light curves. The latter shows a clear plateau which gradually steepens due to the concavity of the SSC component. On the other hand, the optical light curve shows the 'standard' unbroken power-law behavior until $t \sim 5 \times 10^5$ s and flattens off slightly at even later times, as the SSC component takes over.

The above results show that in order the X-ray light curves to show plateaus, at least within the context of our model, the SSC component should be rather flat in the X-ray energy range at the time the synchrotron component decays due to its exponential cutoff. Since the above conditions implicate the magnetic field $B(r)$, and the lower and upper cutoffs of the electron injection, $\gamma_{\rm min}$ and $\gamma_{\rm max}$ respectively, one can quantify the above conditions using the parameters of the standard afterglow model. We proceed to do this in the next section.

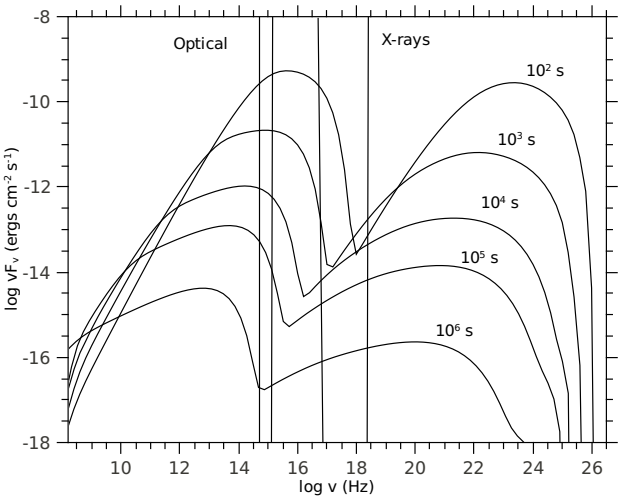

Fig. 2. Multiwavelength spectra at observer times from 10^2 s to 10^6 s (top to bottom). For the parameters used see text. X-ray and optical windows that correspond to the observing energy ranges of XRT $(0.3-10)$ keV and UVOT $(170-650)$ nm respectively, are also shown.

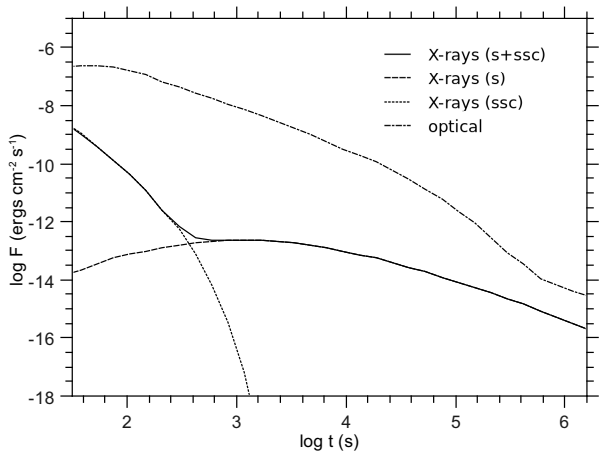

Fig. 3. X-ray (solid line) and optical (dashed-dotted line) light curve corresponding to the same case as in Fig.2. The contribution of the synchrotron (dashed line) and SSC (dotted line) components to the total X-ray flux are also shown. The optical light curve is shifted by +2.5 units in logarithm for reasons of better display.

3. Effects of $\gamma_{\rm max}$

The upper limit of the electron distribution $\gamma_{\rm max}$ has not been so far considered in GRB afterglow models as a dynamic parameter. In this section we will show how a relatively low $\gamma_{\rm max}$ can affect the MW spectra and the corresponding X-ray and optical light curves. We assume that the afterglow is produced by an adiabatic relativistic blast wave decelerating while interacting with the ISM. During this phase the evolution of the RBW is described by the self-similar solution of Blandford & McKee (1976):

$$\Gamma(r) = \Gamma_0 \left(\frac{r}{R_d}\right)^{-3/2} \qquad \text{if } r > R_d, \tag{1}$$

where

$$R_d = \left(\frac{3E_0}{4\pi n_0 m_p c^2 \Gamma_0^2}\right)^{1/3}. \quad (2)$$

Using the relation

$$\int_{t_0}^{t} \mathrm{dt} = \int_{\mathrm{r}_0}^{\mathrm{r}} \frac{\mathrm{dr}'}{2\mathrm{c}\Gamma^2(\mathrm{r}')} \quad (3)$$

and neglecting the term $t_\mathrm{d} = \frac{R_\mathrm{d}}{2c\Gamma_0^2}$ compared to $\int_{R_\mathrm{d}}^{r} \frac{\mathrm{dr}'}{2c\Gamma^2(r')}$ we find that

$$r \approx (8ct\Gamma_0^2 R_d^3)^{1/4}. \quad (4)$$

For the strength of the magnetic field (in the fluid frame), we adopt the usual form

$$B(r) = \sqrt{32\pi n_0 m_p \epsilon_\mathrm{B}}\, c\Gamma(r). \quad (5)$$

The observed synchrotron frequency corresponding to γ_max is given by:

$$\begin{aligned}\nu_{\mathrm{s,max}} &= \Gamma \frac{eB}{2\pi m_e c}\gamma_\mathrm{max}^2 \\ &= \left(\frac{3E_0 n_0 m_p \epsilon_\mathrm{B}^2 e^4}{32\pi^3 c^5 m_e^4}\right)^{1/4} \gamma_\mathrm{max}^2 t^{-3/4}. \end{aligned} \quad (6)$$

We consider an X-ray window that corresponds to the observing energy range of XRT, i.e $(0.3-10)$ keV. We are interested in the time $t_\mathrm{coff,s}^{(\mathrm{x})}$ when photons belonging to the synchrotron exponential cutoff which forms above $\nu_\mathrm{s,max}$ (see Fig. 1) cross a characteristic frequency of the X-ray band, say $\nu_\mathrm{x} \approx 6.3\times 10^{17}$ Hz. So we set $\nu_\mathrm{s,coff} = A\nu_\mathrm{s,max}$ where A is a numerical factor of order $5-10$ which determines how deep into the exponential cutoff the particular synchrotron photons are. Then the expression for $t_\mathrm{coff,s}^{(\mathrm{x})}$ becomes

$$t_\mathrm{coff,s}^{(\mathrm{x})} \approx \left(\frac{3E_0 n_0 m_p \epsilon_\mathrm{B}^2 e^4}{32\pi^3 c^5 m_e^4}\right)^{1/3} \nu_\mathrm{x}^{-4/3} A^{4/3} \gamma_\mathrm{max}^{8/3}. \quad (7)$$

Demanding that the characteristic time $t_\mathrm{coff,s}^{(\mathrm{x})}$ lies in a time interval of the general form:

$$t_k \le t_\mathrm{coff,s}^{(\mathrm{x})} \le t_{k+1}, \quad (8)$$

where $t_k = 10^k$ s, equations (7) and (8) combine to give the first constraining relation for γ_max:

$$g_1(E_0, n_0, \epsilon_\mathrm{B}) \le \gamma_\mathrm{max} \le g_2(E_0, n_0, \epsilon_\mathrm{B}), \quad (9)$$

where $g_{1,2}(E_0, n_0, \epsilon_\mathrm{B}) = C_{1,2}\, 10^{3k/8}\, A^{-1/2} E_{0,54}^{-1/8} n_{0,0}^{-1/8} \epsilon_{\mathrm{B},-2}^{-1/4}$ with $C_1 = 4.1\times 10^3$ and $C_2 = 9.7\times 10^3$. One should keep in mind that relation (8) is valid only for values of the real variable k which ensure that time t_k is larger than the deceleration time t_d. Here and throughout the text, the convention $Q_x \equiv Q/10^x$ has been adopted in cgs units. It is worth noting that for typical values of $E_{0,54} = n_{0,0} = \epsilon_{\mathrm{B},-2} = 1$ and $k = 2$ the maximum electron Lorentz factor lies between 8.1×10^3 and 1.9×10^4, which is relatively low. Although the above double inequality involves three free parameters of the model, the dependence on two of them, i.e on E_0 and n_0 is very weak.

The SSC component peaks at a characteristic frequency which depends on the Compton logarithm first introduced by Gould (1979). In the simple case where the electron distribution is given by a pure power law between γ_min and γ_max and the scatterings happen in the Thomson regime, it is found that the peak frequency of the SSC component is $\nu_\mathrm{p} = \frac{4}{3}\gamma_\mathrm{max}^2 \nu_\mathrm{s,min}$ (see Appendix for a detailed calculation). In a generic case where the electron distribution shows a cooling break, the calculation of the SSC peak frequency is more complicated (see discussion in §2.2). However, in all cases the minimum frequency of the main SSC branch, i.e $\nu_\mathrm{ssc,min} = \frac{4}{3}\gamma_\mathrm{min}^2 \nu_\mathrm{s,min}$ is below (slow cooling regime) or at least equal (fast cooling regime) to the peak frequency. For that reason we choose to quantify the lower energy part of the SSC component as $b\nu_\mathrm{ssc,min}$, where b is a numerical factor of order $0.001-0.01$. In order to proceed we need to use an expression for γ_min. So far in GRB afterglow models, γ_max was not treated as a 'dynamic' parameter in the sense, that its signature would not be observed in the X-ray energy range and below, as it was taken to be much larger than γ_min. For that reason the approximate expression for γ_min (Sari et al. 1998)

$$\gamma_\mathrm{min}^\mathrm{approx} = \epsilon_\mathrm{e}\frac{m_\mathrm{p}}{m_\mathrm{e}}\frac{p-2}{p-1}\Gamma(r) \quad (10)$$

was safely used. However, in our work where we also examine cases with γ_max only a few times greater than γ_min, in the numerical code we use the accurate expression which is solution to the equation:

$$\frac{\gamma_\mathrm{min}^{2-p} - \gamma_\mathrm{max}^{2-p}}{\gamma_\mathrm{min}^{1-p} - \gamma_\mathrm{max}^{1-p}} = \epsilon_\mathrm{e} f_p \frac{m_\mathrm{p}}{m_\mathrm{e}}\Gamma(r), \quad (11)$$

where $f_p = \frac{p-2}{p-1}$. As the solution to the equation above has no explicit analytical form, we proceed first to find a constraint of γ_max using the approximate analytical expression given by eq. (10). For the low energy part of the SSC component we can now write:

$$\begin{aligned} b\nu_\mathrm{ssc,min} &\approx \frac{2eb}{3\pi m_e}\sqrt{32\pi n_0 m_p \epsilon_\mathrm{B}}\left(\epsilon_\mathrm{e}\frac{m_p}{m_e}f_p\right)^4 \cdot \\ &\cdot \left(\frac{3E_0}{2048\pi n_0 m_p c^5}\right)^{3/4} t^{-9/4}. \end{aligned} \quad (12)$$

In order to have a flattening of the light curve after the first break, this low energy part of the SSC component must appear in the X-ray band about the time when the synchrotron one decays. In complete analogy to $t_\mathrm{coff,s}^{(\mathrm{x})}$, the observed time $t_\mathrm{ssc}^{(\mathrm{x})}$ at which the frequency $b\nu_\mathrm{ssc,min}$ enters the X-ray band is determined by the relation

$$\begin{aligned} t_\mathrm{ssc}^{(\mathrm{x})} &= \nu_\mathrm{x}^{-4/9}\left(\frac{2eb}{3\pi m_e}\right)^{4/9}(32\pi n_0 m_p \epsilon_\mathrm{B})^{2/9}\left(\epsilon_\mathrm{e}\frac{m_p}{m_e}f_p\right)^{16/9} \cdot \\ &\left(\frac{3E_0}{2048\pi n_0 m_p c^5}\right)^{1/3}. \end{aligned} \quad (13)$$

The ratio of the two characteristic times is given by:

$$\frac{t^{(\mathrm{x})}_{\mathrm{ssc}}}{t^{(\mathrm{x})}_{\mathrm{coff,s}}} = \left[\left(\nu_{\mathrm{x}}\frac{m_p}{m_e}\right)^2\frac{\pi m_p}{6e^2}\right]^{4/9} b^{4/9}A^{-4/3}\gamma_{\mathrm{max}}^{-8/3}\left(\frac{f_p^4\epsilon_{\mathrm{e}}^4}{n_0\epsilon_{\mathrm{B}}}\right)^{4/9} \quad (14)$$

$$\approx 2\times 10^{16}\; b^{4/9}A^{-4/3}\gamma_{\mathrm{max}}^{-8/3}\left(\frac{f_p^4\epsilon_{\mathrm{e}}^4}{n_0\epsilon_{\mathrm{B}}}\right)^{4/9}. \quad (15)$$

When the two timescales $t^{(\mathrm{x})}_{\mathrm{coff,s}}$ and $t^{(\mathrm{x})}_{\mathrm{ssc}}$ are of the same order, a break will appear in the X-ray light curve, as the synchrotron component gives its place to the low energy part of the SSC one. Allowing

$$0.2 < \frac{t^{(\mathrm{x})}_{\mathrm{ssc}}}{t^{(\mathrm{x})}_{\mathrm{coff,s}}} < 1.0 \quad (16)$$

we obtain one more constrain for γ_{max}, i.e.

$$h_1(n_0,\epsilon_{\mathrm{e}},\epsilon_{\mathrm{B}},f_p) < \gamma_{\mathrm{max}} < h_2(n_0,\epsilon_{\mathrm{e}},\epsilon_{\mathrm{B}},f_p), \quad (17)$$

where the functions $h_{1,2}$ are defined as $h_{1,2} = K_{1,2}\; A^{-1/2}b^{1/6}f_p^{2/3}\epsilon_{\mathrm{e},-1}^{2/3}n_{0,0}^{-1/6}\epsilon_{\mathrm{B},-2}^{-1/6}$ with $K_1 = 6\times 10^5$ and $K_2 = 1.1\times 10^6$. The above relations make the tacit assumption that the scatterings occur in the Thomson regime, at least for the lower energy part of the SSC spectrum. For that reason, we impose one more constraint on γ_{max} demanding that at least for $t\sim t^{(\mathrm{x})}_{\mathrm{coff,s}}$ the assumption of scattering in the Thomson regime is valid. For that we use the dimensionless factor

$$x = \frac{\gamma_{\mathrm{min}}h\nu'_{\mathrm{s,min}}}{m_ec^2} = \frac{\hbar e}{8m_e^2c^2}\left(\frac{3E_0\epsilon_{\mathrm{B}}}{c^5}\right)^{1/2}\left(f_p\frac{\epsilon_{\mathrm{e}}m_p}{m_e}\right)^3 t^{-3/2}, \quad (18)$$

where primed quantities are measured in the comoving frame. At $t = t^{(\mathrm{x})}_{\mathrm{coff,s}}$ the x parameter is given by:

$$x = \frac{\hbar f_p^3m_p^3}{8em_e^3c^2}\left(\frac{32\pi^3}{m_p}\right)^{1/2}\nu_{\mathrm{x}}^2\;\epsilon_{\mathrm{e}}^3A^{-2}\gamma_{\mathrm{max}}^{-4}(n_0\epsilon_{\mathrm{B}})^{-1/2}. \quad (19)$$

Thus, when $x<1$ we find that:

$$\gamma_{\mathrm{max}} \gtrsim 50\; A^{-1/2}n_{0,0}^{-1/8}f_p^{3/4}\epsilon_{\mathrm{e},-1}^{3/4}\epsilon_{\mathrm{B},-2}^{-1/8}. \quad (20)$$

The above relation for typical parameter values poses only a weak constraint on γ_{max}. The same holds even if the accurate expression for γ_{min} was used. For that reason from here on we will not take into consideration the constraining relation (20).

Having determined the constraining relations for γ_{max} using the approximate form of γ_{min}, we can now estimate the corrections introduced, after taking into account the accurate expression of it. For the purposes of our analytic analysis we model it as:

$$\gamma_{\mathrm{min}} = f_{\mathrm{mod}}\gamma_{\mathrm{min}}^{\mathrm{approx}}, \quad (21)$$

where the term f_{mod} is a function of the radius r and of the ratio $\frac{\gamma_{\mathrm{max}}}{\gamma_{\mathrm{min},0}}$; $\gamma_{\mathrm{min},0}$ is the initial minimum Lorentz factor of the electrons. Function f_{mod} is plotted, for illustrative reasons, against radius r for two values of $\frac{\gamma_{\mathrm{max}}}{\gamma_{\mathrm{min},0}}$ in Fig. 4. It is evident that $f_{\mathrm{mod}}\to 1$ in the limit of $\gamma_{\mathrm{max}} >> \gamma_{\mathrm{min},0}$, as expected. As our analysis holds for the deceleration phase of the RBW, we can simplify the calculations further by averaging the function f_{mod} over $\tilde{r} = \log r$ for $r > R_d$:

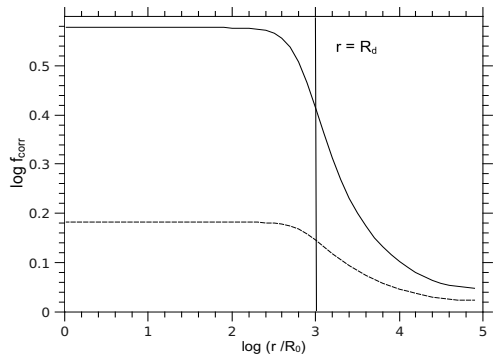

Fig. 4. Log-Log plot of f_{mod} as a function of radius r (in units of the initial radius $R_0 = 10^{14}$ cm) for two values of the ratio $\frac{\gamma_{\mathrm{max}}}{\gamma_{\mathrm{min},0}}$: 1.32 (solid line) and 33 (dashed line). Other parameters used are: $E_0 = 10^{54}$ ergs, $\Gamma_0 = 400$, $n_0 = 1$ part/cm^3, $\epsilon_{\mathrm{B}} = 0.001$, $\epsilon_{\mathrm{e}} = 0.01$ and $p = 2.3$. The deceleration radius is also shown.

$$\bar{f}_{\mathrm{mod}}\left(\frac{\gamma_{\mathrm{max}}}{\gamma_{\mathrm{min},0}}\right) = \frac{\int_{r>R_d}d\tilde{r}\,f_{\mathrm{mod}}\left(\tilde{r},\frac{\gamma_{\mathrm{max}}}{\gamma_{\mathrm{min},0}}\right)}{\int_{r>R_d}d\tilde{r}}. \quad (22)$$

This average modifying parameter can be used in eq. (21) instead of f_{mod}. Thus, constraining relation (17) becomes:

$$\bar{h}_1 < \gamma_{\mathrm{max}} < \bar{h}_2, \quad (23)$$

where $\bar{h}_{1,2} = \bar{f}_{\mathrm{mod}}^{\;2/3}h_{1,2}$. Table 1 shows some indicative values of the correction introduced in relation (23) for $E_0 = 10^{54}$ ergs, $\Gamma_0 = 400$, $n_0 = 1$ part/cm^3, $\epsilon_{\mathrm{B}} = 0.001$ $\epsilon_{\mathrm{e}} = 0.01$ and $p = 2.3$.

$\log\gamma_{\mathrm{max}}$	$\log(\gamma_{\mathrm{max}}/\gamma_{\mathrm{min},0})$	$\frac{2}{3}\log\bar{f}_{\mathrm{mod}}$
4.15	0.495	0.087
4.35	0.787	0.072
5.35	2.00	0.030

Table 1. Indicative values of the correction introduced in the constraining relation (23). For the parameters used see text.

Using eq. (9) and (23) we can plot γ_{max} versus ϵ_{e} for fixed values of E_0, n_0, p and ϵ_{B}, creating a parameter space shown in Fig. 5. The other parameters used are the same as those used in Table 1 above. The curves defined by eq. (9) and (23) create distinctive areas on the parameter space. For initial values chosen from the striped area, eq. (11) has as solution $\gamma_{\mathrm{min},0} = \gamma_{\mathrm{max}}$ with no physical meaning. In that sense the striped area is not permitted. The horizontal zones labeled by $k = 2$ and $k = 3$ are related to cases where the transition time $t^{(\mathrm{x})}_{\mathrm{coff,s}}$ lies between $10^2 - 10^3$ s and $10^3 - 10^4$ s respectively. A choice of $k < 2$ would correspond to breaks occuring at even earlier times. We call a 'plateau

strip' the tilted zone, as a choice of a pair $(\epsilon_e, \gamma_{\max})$ from it leads to X-ray light curves which show a shallow decline phase, i.e a 'plateau'. Moreover, if this pair is chosen from the intersection of the 'plateau strip' with a horizontal zone labeled by $k = 2$ for example, the plateau phase will begin at a time between $10^2 - 10^3$ s and so on. Finally, a choice of pairs from the area outside the tilted zone leads to X-ray light curves with a single change of slope.

For a better inspection of the parameter space, we have chosen pairs from four distinctive regions of the diagram and show the corresponding X-ray and optical light curves in Figs. 6 and 8. As we move from point 1 to 2, i.e by increasing ϵ_e while keeping $\gamma_{\max}$ constant, the break times (see Fig. 6) remain constant while the light curve shapes exhibit a transition as the decay becomes flatter leading to a plateau phase. From point 2 to 3, the break is shifted towards later times while the light curve becomes, once again steep. This is to be as expected since point 3 lies outside the 'plateau strip'. Finally, as we move from point 3 to 4 the slope of the light curve after the break becomes flat and a plateau is produced. This behavior is the same with the already discussed transition from point 1 to 2, with the sole exception that now the break occurs at later times. Note that for all the numerical runs presented in the present work, we use the accurate expression for $\gamma_{\min}$ by solving eq. (11). For that we have included in our numerical code a subroutine that utilizes a combination of the bisection and Newton-Raphson Method (Press et al. 1992).

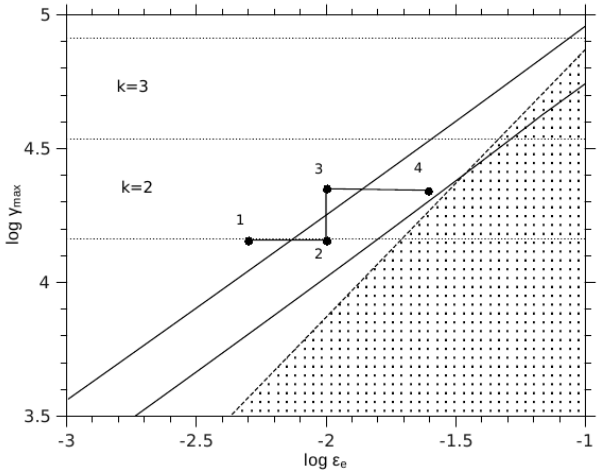

Fig. 5. Initial value parameter space of $\gamma_{\max}$ and ϵ_e for $E_0 = 10^{54}$ ergs, $\Gamma_0 = 400, n_0 = 1$ part/cm^3, $\epsilon_B = 0.001$ and $p = 2.3$. The numerical factors chosen here are $A = 8, b = 0.001$ (see text for their definition). Dotted lines correspond to the constraining relation (9), solid lines to (23) and the dashed line sets the boundary of the striped area, which is not permitted as it it leads to $\gamma_{\max} = \gamma_{\min,0}$. The horizontal zones labeled by $k = 2$ and $k = 3$ correspond to transition times $t^{(x)}_{\rm coff,s}$ lying in the time intervals $10^2 - 10^3$ s and $10^3 - 10^4$s respectively. The 'coordinates' $(\epsilon_e, \gamma_{\max})$ of the points 1 to 4 marked on the plot are: $\{(0.005, 1.41 \times 10^4),\ (0.01, 1.41 \times 10^4),\ (0.01, 2.24 \times 10^4),\ (0.025, 2.24 \times 10^4)\}$ respectively . The corresponding X-ray and optical light curves of the aforementioned points are presented in the following Figs. 6 and 8.

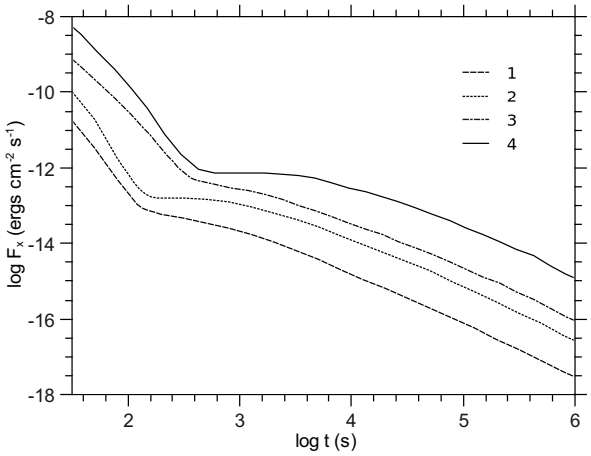

Fig. 6. X-ray light curves for different set of parameters corresponding to the points from 1 to 4 (bottom to top) marked on panel (b) of Fig. 5. The first break of the X-ray light curves 1 and 2 occurs at around 125 s, while for the light curves 3 and 4 occurs later at $t \sim 650$ s. For clarity reasons light curves 1, 3 and 4 are plotted with an offset of -0.2, $+0.4$ and $+0.5$ in logarithmic units of flux respectively.

One could also make some comments on the effects of the other free parameters, which were assumed fixed in Fig. 5, will have on the parameter space. For example, a possible change of E_0 will affect only the dotted lines in Fig. 5. The effect will not be of great importance as the inequality (9) has a very weak dependance on E_0. In general, an increase of ϵ_B will shift the 'plateau strip' downwards. Although the parameter Γ_0 does not appear explicitly in the constraining relations (9) and (23) has an effect on the relative positions of the striped area and the 'plateau strip'. Finally, the external number density n_0 may not affect severely the appearance of the parameter space, but has an important effect on the ratio of the synchrotron to the SSC flux. We note that as it was shown in PM09, an increase of n_0 makes the afterglow more Compton dominated. This possibility has also been discussed by Panaitescu & Kumar (2000) and Sari & Esin (2001). A denser external medium, increases in νF_ν units the X-ray flux over the optical. Such high values of external density are required by our model in cases where the X-ray light curve shows a shallow phase and the ratio $L_X/L_{\rm opt} > 1$. Figure 7 shows such a case. The parameters used are $E_0 = 10^{54}$ ergs, $\Gamma_0 = 100$, $n_0 = 10^3$, $\epsilon_B = 10^{-5}$, $\epsilon_e = 0.032$ and $\gamma_{\max} = 8.2 \times 10^4$. For $t > 10^3$ s, when the spectral eivolution in the X-ray energy band is not very important, the optical flux lies approximately one order of magnitude below the X-ray one.

As the RBW decelerates the synchrotron and SSC emission from the forward shock becomes weaker and softer (see Fig. 2). As a result, the synchrotron cutoff will enter at some instant $t^{(\rm opt)}_{\rm coff,s}$ in the optical band. It is straightforward to show, under the assumptions of the problem, i.e. when $B \propto r^{-3/2}$ and $\gamma_{\max}$ independent of r, that this is related to $t^{(x)}_{\rm coff,s}$ by:

$$t^{(\rm opt)}_{\rm coff,s} = \left(\frac{\nu_x}{\nu_{\rm opt}}\right)^{4/3} t^{(x)}_{\rm coff,s} \qquad (24)$$

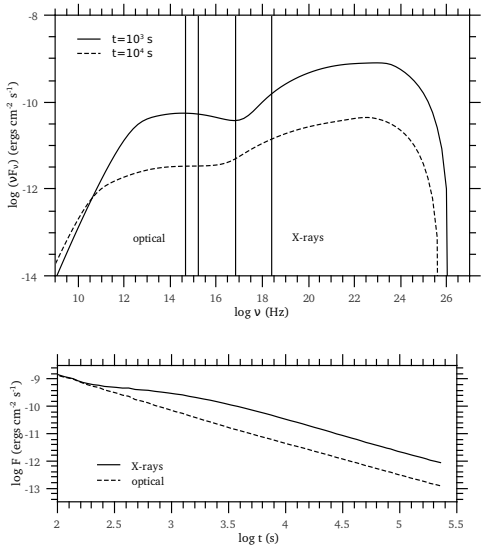

Fig. 7. Multiwavelength spectra at observer times 10^3 s and 10^4 s (top) and light curves for the X-ray and optical band (bottom) for an SSC dominated afterglow. For the parameters used see text. The X-ray and optical windows are as given in Fig. 2.

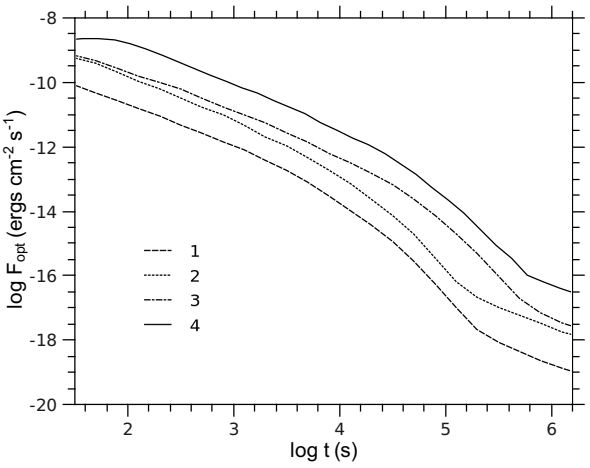

Fig. 8. Optical light curves for different set of parameters corresponding to the points 1 to 4 (bottom to top) marked on panel (b) of Fig. 5. For clarity reasons light curves 1, 3 and 4 are plotted with an offset of -0.4, $+0.2$ and $+0.5$ in logarithmic units of flux respectively.

or, equivalently, by

$$t_{\rm coff,s}^{\rm (opt)} \approx 2\times 10^3\, t_{\rm coff,s}^{\rm (x)}, \qquad (25)$$

where a typical optical frequency $\nu_{\rm opt} = 2\times 10^{15}$ Hz was used. For the cases represented by points 1 and 2 in Fig. 5 one finds $t_{\rm coff,s}^{\rm (x)} \approx 125$ s (see also Fig. 6). Thus, a break in the optical light curve is expected at around 2.5×10^5 s, which is confirmed numerically and it is shown in Fig. 8. The other two optical light curves in the same figure show a break at correspondingly later times ($\gtrsim 6.3\times 10^5$ s). We should also note that the break of the optical light curve will not neccessarily be of a 'plateau' type. This is due to the fact that the emerging SSC component has become steeper since the time it has emerged in the X-ray window (see Fig. 2 for the time evolution of the SSC component). A natural outcome of our model is that the optical light curves do not exhibit a break during the plateau phase of the corresponding one in X-rays, as it was first noted by Fan & Piran (2006). Evidence for chromatic breaks in X-ray light curves were also discussed in Panaitescu et al. (2006).

Chromatic breaks in the optical and X-ray light curves can be produced by our model with an expected time difference given by eq. (25). As we discuss in the last section, this is a strong constrain which reflects the validity of the model's assumptions.

4. Basic results

It is well known that the X-ray and optical light curves of GRB afterglows show a wide range of behaviors. Especially in the X-ray regime (Nousek et al. 2006; Evans et al. 2009) the behavior can be quite perplexing (see Fig. 9) with many cases showing a plateau which is quite difficult to interpret within the context of the standard model. The analysis performed in §3 can tentatively be of some relevance to these observations. Using, for instance the example set by Fig. 5 as a guide, we can say that plateaus appear as long as the values of $\gamma_{\rm max}$ and $\epsilon_{\rm e}$ are chosen from the region defined by the two tilted lines. Moving inside this region from the lower left to the upper right, plateaus appear at progressively longer times. Furthermore, a choice of the initial parameters outside this region (for example, from the left top corner of Fig. 5) leads to afterglows without a plateau phase. Fig. 10 shows different types of X-ray light curves obtained using our numerical code corresponding to points from different regions of the parameter space of Fig. 5. Light curves in panels (a) and (b) correspond to points (4) and (1) already shown in Fig. 5, while light curves of panels (c) and (d) are obtained using $(\epsilon_{\rm e},\gamma_{\rm max}) = (0.0032, 6.3\times 10^3)$ and $(0.01, 10^6)$ respectively.[1] A tentative comparison of our model light curves to those of Fig. 9 can be made.

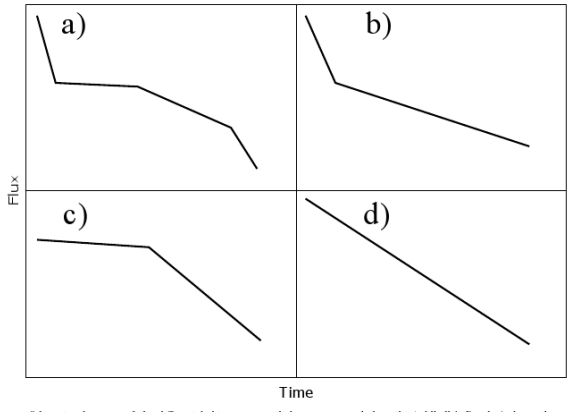

Fig. 9. Schematic diagram from Evans et al. (2009) showing the different light curve morphologies observed.

As the model presented here produces multiwavelength spectra at each instant, we can use it to calculate the evo-

[1] All other parameters used are the same as in Fig. 5 except for the case presented in panel (c) where $\Gamma_0 = 800$ was used.

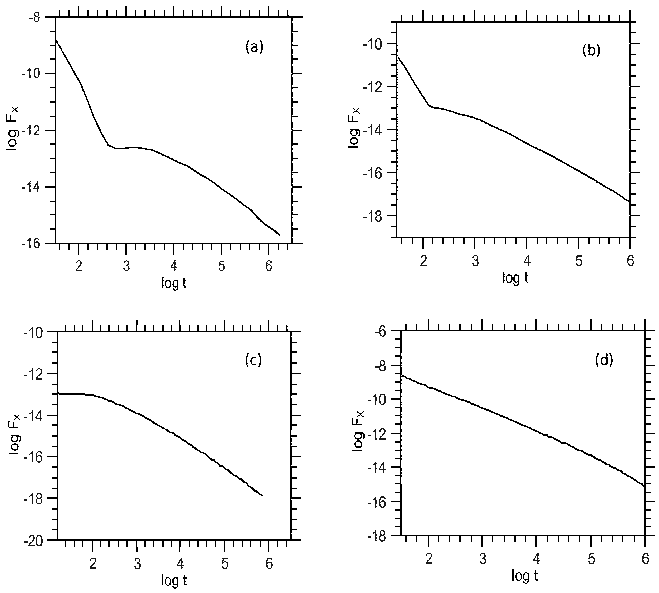

Fig. 10. Different light curve morphologies obtained using our numerical code corresponding to points from different regions of the parameter space shown in Fig. 5. Light curves from each panel can be tentatively compared to the corresponding ones of Fig. 9. For the parameters used see text.

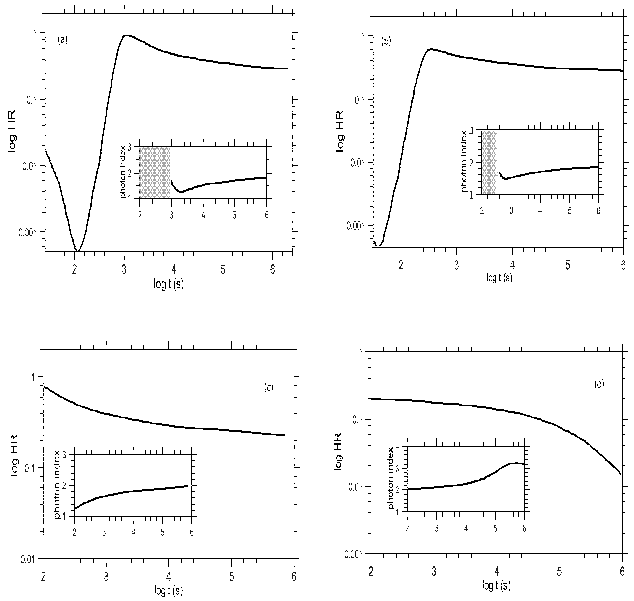

Fig. 11. Time evolution of the hardness ratio for each of the cases presented in Fig. 10. For the definition of the hardness ratio used see text. The insert in each panel shows the evolution of the corresponding photon index. The shaded areas in the inserts imply that during this period our model spectra cannot be approximated by a single power law and therefore a specific photon index could not be attributed to the spectrum.

lution of the expected X-ray hardness ratio defined as the ratio of counts in the 1.5-10 keV to the counts in the 0.1-1.5 keV band (Evans et al. 2009, 2010). Figure 11 shows the time evolution of the hardness ratio for each of the example cases shown in Fig. 10. Time evolution of the corresponding photon index is also shown in the inserts of Fig. 11, whenever the spectral shape allows its viable calculation at the particular time (for a more detailed discussion on the shape of our X-ray model spectra see §2).

For X-ray light curves with a distinctive 'plateau' phase, we find that the spectral evolution shows a characteristic trend as the X-ray window is first dominated by the synchrotron and later by the SSC component. This can be seen in panel (a) of Fig. 11. At very early times both the soft and hard X-ray bands are dominated by the synchrotron photons – however the hard band is affected first by the synchrotron cutoff and this has as a result the decrease of the hardness ratio. During this phase the spectrum in X-rays is shaped by an exponential cutoff (synchrotron emission) and an emerging flat power law component (SSC emission). Thus, it cannot be simply approximated by a single power law and 'labeled' by a photon index (shaded area in the insert). At later times, the SSC component starts appearing in the hard band while the decreasing synchrotron component dominates the soft one, resulting in an increase of the hardness ratio. Finally, at even later times both bands are dominated by the SSC component, whose low energy part can be approximated by a flat power law, and due to its gradual steepening the hardness ratio appears to decrease gently.

In cases where the X-ray flux decays as a power law with time, as in panel (d) of Fig. 10, we find no significant spectral evolution. The photon index is approximately constant almost for three or four decades in time, as the power law segment of the synchrotron component dominates until late times in the X-rays (see insert in panel (d) of Fig. 11). The other two cases presented in panels (b) and (c) of Fig. 11 lie somewhere inbetween the two aforrementioned example cases.

Although the qualitative evolution of the photon index with time is a robust feature of our model , its specific value depends on the value of the other model parameters, such as the slope of the electron energy spectrum. In all our runs we have used a typical value of $p = 2.3$.

5. Summary/Discussion

In the present paper we have investigated the role that the upper cutoff of the electron injection can play in the evolution of the multiwavelength spectra and light curves of GRB afterglows. For this we have solved self-consistently the kinetic equations that govern the electron evolution and photon radiation as a function of distance (see also Fan et al. (2008) and PM09). This approach can address successfully the effects of the electron cutoff radiation on the light curves.

We have shown that depending on the adopted value of $\gamma_{\rm max}$ the X-ray lightcurves can show one of the following behaviours:

1. In cases where $\gamma_{\rm max}$ is not much greater than the lower cutoff $\gamma_{\rm min}$, the X-ray light curves show three distinct phases. First a fast drop phase which corresponds to the exponential cutoff of the synchrotron component. Then a plateau phase which is caused from the gradual dominance of the SSC component over the decaying synchrotron. Finally, a more gradual power-law decay which corresponds to the normal evolution of the SSC component. The analytical approach used in §3 and

summarized in Fig. 5 shows that, depending on the initial parameters, there might be a narrow strip in phase space that produces X-ray plateaus. In all cases we found that $\gamma_{\rm max}$ should be no more than a factor of 10 larger than $\gamma_{\rm min}$.

2. If $\gamma_{\rm max}$ does not satisfy the above condition but it is still close to the 'plateau strip', then the X-ray afterglows do not show a plateau but simply a change in the power law decay, i.e. the three phases degenerate into two.

3. In cases where $\gamma_{\rm max} \gg \gamma_{\rm min}$ we find that the X-ray afterglows will be dominated until very late times by the synchrotron component, i.e. we obtain the standard afterglow picture.

These trends are exemplified in Figures 6 and 10. As far as the flux decay in the optical regime is concerned, the present model predicts that the optical light curve will mimic the X-ray one with two major differences (see Fig. 8). First, the break in the optical light curve will come at much later times (see eq.(25)) and second, after the break, the optical light curve will not neccessarily show a plateau. Note however, that both of these statements are based on the assumption that $\gamma_{\rm max}$ remains constant throughout the RBW evolution.

In this respect, $\gamma_{\rm max}$ emerges as one of the important parameters of the afterglow evolution as its choice can control critically the behaviour of the X-ray light curves.

The evolution of the X-ray hardness ratio and spectral indices were presented in Fig 11. Our model derived hardness ratio shows a characteristic signature which is compatible with observations at least during the early stages (Butler & Kocevski 2007; Liang et al. 2007). On the other hand it is still inconclusive regarding the late stages (P. O'Brien – private communication), as the transition from the plateau to the normal decay shows an evolution in the hardness ratio by a factor of two, which is not the case for several individual GRBs (e.g. Vaughan et al. (2006); Liang et al. (2007)). However, as preliminary calculations have shown (Petropoulou, Mastichiadis & Piran (2011) – to appear in the proceedings of the 25$^{\rm th}$ Texas Symposium held last December in Heidelberg), this is greatly relaxed in the case where $\gamma_{\rm max}$ is allowed to increase with radius. As the study of such cases is beyond the scope of the present paper, we will treat this in a forthcoming publication.

It is important to emphasize at this point that the close relation we found between X-ray light curves exhibiting a plateau phase and a $\gamma_{\rm max}$ not much greater than $\gamma_{\rm min}$, is what actually differentiates our model from other works (e.g. long lasting energy injection into the forward shock - refreshed shock models (Zhang et al. 2006), late prompt emission (Ghisellini et al. 2007; Ghisellini 2008), geometrical effects (Eichler & Granot 2006; Granot et al. 2006), non-standard deceleration of the bulk Lorentz factor due to the Compton-drag force (Mastichiadis & Kazanas 2009), dust scattering (Shao et al. 2008) and others). Some recent PIC simulations show that most of the particles are accelerated into a relativistic Maxwellian, while a small fraction of them is injected to a power law high energy tail, whose high energy cutoff is approximately only one order of magnitude larger than the low one (Spitkovsky 2008; Sironi & Spitkovsky 2009). However, this is not a final result, as the present numerical simulations have not reached yet a steady state, where $\gamma_{\rm max}$ is expected to be larger than the one found so far. It is interesting to note also that when we set $\gamma_{\rm max}$ not much larger than $\gamma_{\rm min}$ the qualitative behavior of our results is similar to the one obtained when one replaces the power law injection with a relativistic Maxwellian (Giannios & Spitkovsky 2009). All other parameters used in our work are the same as in the standard GRB afterglow model.

Spectral evolution during the steep early phase, which is observed in a significant number of GRB afterglows (see Zhang et al. (2007) for a systematic study of 44 steeply decaying X-ray afterglows), is an inevitable outcome of our model, as in our present work the early steep decay of the X-ray light curve is atrributed to the emission from the external shock. Moreover there is some observational evidence for a possible smooth connection of the early afterglow to the prompt emission (Barthelmy et al. 2005). In such a case the present work could be seen as an extension of the supercritical model (Mastichiadis & Kazanas 2009) to the afterglow regime. Alternatively it can result from a gradual transition towards the end of the prompt phase to an external shock emission. Evidence for such a transition is seen in several examples where the extrapolated BAT light curve is not connected to early-time XRT light curve (Tagliaferri et al. 2005). This fact combined with a strong spectral evolution at early times suggests that the two emissions are produced by either different mechanisms or in different regions. Such a transition from the prompt to the afterglow emission could be explained within the context of the internal/external shock scenario (Piran (1999, 2004)– see also Dermer (2007) for a discussion on the possible scenarios).

Finally we would like to present potentially problematic points of our model – some of these could be addressed with future observations and further analysis.

1. In the case of an afterglow with a plateau phase we find that the X-ray spectrum cannot be represented by a simple power-law during the steep decay-early plateau phase. The spectral shape at this stage can more accurately be described by a steep component coming from the synchrotron cutoff plus a flat power-law coming from the emerging SSC component – see Fig. 2 at early times.

2. Some preliminary efforts in fitting lightcurves and hardness ratios [2] have shown that, in some cases, our model can successfully reproduce both (e.g. GRB 060512 – see Petropoulou et al. 2011). However, in other cases the model can fit successfully only the lightcurve while the HR fit is poorer (e.g. GRB 050713B).

3. If the light curve shows an abrupt break (either a plateau phase or a single change in the slope decay) and $L_X/L_{\rm opt} > 1$, then our model requires high values of the external density ($n \geq 100$ cm^{-3}). This could be problematic in cases of GRB afterglows for which low values of N_H are derived (Schady et al. 2007). We note

[2] Although a successfully fit of the HR could mot neccessarily mean a succesful spectral fit, we preferred to model the former than the latter as in many cases our X-ray spectra cannot be reproduced well by a single power-law – see also the previous point.

however that, in all other cases the above constrain of our model is relaxed.

4. For those GRBs where the early steep decay is smoothly connected to the prompt emission phase, the model requires that the late prompt emission is already dominated by an external shock emission. This arises naturally in the external shock model or it requires a transition, during the late prompt phase , from in the internal to external shock.

Concluding we could say that the consideration of the electron distribution's upper energy cutoff as another free parameter in the standard afterglow model brings many interesting features in the light curve / spectral behavior of GRB afterglows. All these are related to the evolution of the relativistic electron distribution and eventually point out at the acceleration mechanism at work. We plan to deal with this issue in a forthcoming publication.

Acknowledgements. AM would like to thank TP for hospitality during a visit in Hebrew University. We thank Drs. P. Evans, P. O'Brien and A. Zezas for useful discussions and Dr. D. Giannios for comments on the manuscript. This work made use of data supplied by the UK Swift Science Data Centre at the University of Leicester. This research has been co-financed by the European Union (European Social Fund - ESF) and Greek national funds through the operational Program 'Education and Lifelong Learning' of NSRF - Research Funding Program: Heracleitus II.

Appendix A: Synchrotron Self-Compton spectrum of a power-law electron distribution

We assume a spherically symmetric source of radius R with a magnetic field B randomly oriented. Synchrotron radiation is produced by an isotropic electron distribution, of the form

$$n_{\rm e} = k_{\rm e}\gamma^{-p} \qquad \gamma_{\rm min} < \gamma < \gamma_{\rm max} \tag{A.1}$$

where p is the exponent of the power-law spectrum, $\gamma_{\rm min}, \gamma_{\rm max}$ are the cutoffs of the distribution and $k_{\rm e}$ is a normalization factor that determines the electron density and depends on radius r in the case of an inhomogeneous source. The synchrotron photon production rate per unit energy and per unit volume is then given by

$$\frac{dN_{\rm s}}{d\epsilon dt} = \frac{2e^3}{m_{\rm e}h^2c^2}\left(\frac{3e}{4\pi m_{\rm e}c}\right)^{\frac{p-1}{2}} \alpha(p)\ k_{\rm e}B^{\frac{p+1}{2}}\epsilon^{-\frac{p+1}{2}} \tag{A.2}$$

where $\alpha(p)$ is a combination of Γ - functions (see eq. (4.60) of Blumenthal & Gould (1970)). Equation (A.2) holds for photon energies not close to the low- and high- energy ends of the spectrum - $\epsilon_s\gamma_{\rm min}^2$ and $\epsilon_s\gamma_{\rm max}^2$ respectively, where $\epsilon_s = \frac{eB}{2\pi m_e c}$. The number density of synchrotron photons in the source is given by:

$$n_{\rm s}(\epsilon, r) = t_R\frac{dN_{\rm s}}{d\epsilon dt} = \tilde{n}_{\rm s}(r)\epsilon^{-\frac{p+1}{2}} \tag{A.3}$$

where t_R is the crossing time of the source and $\tilde{n}_{\rm s}$ is the energy independent factor on the right hand side of eq. (A.2). The dependence on radius comes from the quantities k_e and B. The explicit functional form of the photon density can be found in Gould (1979). However, for the calculation of the Compton synchrotron logarithm we can safely proceed using the spatial averaged photon density

$$\bar{n}_{\rm s}(\epsilon) = <\tilde{n}_{\rm s}>\ \epsilon^{-\frac{p+1}{2}} \tag{A.4}$$

where $<\tilde{n}_{\rm s}> = \frac{3}{R^3}\int dr\ r^2\tilde{n}_{\rm s}(r)$. We assume further that the Inverse Compton emissivity is given by a δ - function centered at the mean energy of an upscattered synchrotron photon of energy ϵ

$$j_{\rm ic}(\epsilon_1;\gamma,\epsilon) = A\epsilon_1\delta(\epsilon_1 - 4/3\gamma^2\epsilon) \tag{A.5}$$

where A is a normalization factor. Then the total SSC power per unit energy emitted is found by

$$J_{\rm ic}(\epsilon_1) = \int d\epsilon\ n_{\rm s}(\epsilon, r)\int d\gamma\ N_{\rm e}(\gamma)j_{\rm ic}(\epsilon_1;\gamma,\epsilon) \tag{A.6}$$

In the above equation $N_{\rm e} = K_{\rm e}\gamma^{-p}$ is the total number of electrons per Lorentz factor γ in the source. The normalization factor $K_{\rm e}$ is related to $k_{\rm e}$ through the integral $4\pi\int dr\ r^2k_{\rm e}(r)$. In order to simplify further the calculation of the integral in (A.6) we use the average photon density

$$J_{\rm ic}(\epsilon_1) = AK_{\rm e}\ <\tilde{n}_{\rm s}>\int_{\epsilon_{\rm min}}^{\epsilon_{\rm max}} d\epsilon\epsilon^{-\frac{p+1}{2}} I(\epsilon_1,\epsilon) \tag{A.7}$$

where $\epsilon_{\rm min}$, $\epsilon_{\rm max}$ are the effective minimum and maximum energies of the synchrotron photons and

$$\begin{aligned} I(\epsilon_1,\epsilon) &= \int_{\tilde{\gamma}_{\rm min}}^{\tilde{\gamma}_{\rm max}} d\gamma\ \gamma^{-p}\epsilon_1\delta(\epsilon_1 - \frac{4}{3}\gamma^2\epsilon) \\ &= \frac{1}{2}\left(\frac{\sqrt{3}}{2}\right)^{-p+1}\epsilon_1^{-\frac{p-1}{2}}\epsilon^{\frac{p-1}{2}} \end{aligned} \tag{A.8}$$

for $\frac{4}{3}\tilde{\gamma}_{\rm min}^2\epsilon < \epsilon_1 < \frac{4}{3}\tilde{\gamma}_{\rm max}^2\epsilon$. Strictly speaking, the integral equals to zero for any other value of ϵ_1. However, if one uses the complete expression of the Inverse Compton emissivity, finds that outside this energy range the intensity is highly reduced but not actually zero. The lower limit of integration in (A.8) is determined by the kinematics of the compton scattering and the lower cutoff of the electron distribution, i.e

$$\tilde{\gamma}_{\rm min} = \max[\gamma_{\rm min}, (3\epsilon_1/4\epsilon)^{1/2}]. \tag{A.9}$$

The upper limit of integration is given by

$$\tilde{\gamma}_{\rm max} = \min[\gamma_{\rm max}, {\rm m_e c^2}/\epsilon] \tag{A.10}$$

which takes into account the effect of the Klein-Nishina cutoff. For reasons of simplicity we proceed to the calculation of the SSC spectrum assuming that $\tilde{\gamma}_{\rm min} = \gamma_{\rm min}$ and $\tilde{\gamma}_{\rm max} = \gamma_{\rm max}$.

Appendix B: The Compton-synchrotron logarithm

The integration over the synchrotron photon distribution (see eq. (A.7), (A.8)) leads to a factor

$$\ln\Sigma = \ln\left(\frac{\epsilon_{\rm max}}{\epsilon_{\rm min}}\right) \tag{B.1}$$

called the Compton synchrotron logarithm (Gould 1979). This quantity takes into account the effective minimum

and maximum energies of synchrotron photons, which contribute to the principal branch of the SSC spectrum, i.e to upscattered photons with energies between $\sim \epsilon_s\gamma_{\rm min}^4$ and $\sim \epsilon_s\gamma_{\rm max}^4$. The actual extent of the synchrotron power law segment is

$$\epsilon_s\gamma_{\rm min}^2 < \epsilon < \epsilon_s\gamma_{\rm max}^2 \tag{B.2}$$

where $\epsilon_s = \frac{eB}{2\pi m_e c}$. In the previous section we showed that only for energies of the upscattered synchrotron photons between

$$\frac{4}{3}\gamma_{\rm min}^2\epsilon < \epsilon_1 < \frac{4}{3}\gamma_{\rm max}^2\epsilon \tag{B.3}$$

the SSC spectrum differs significantly from zero. From eq. (B.2), (B.3) we find $\epsilon < \epsilon_s\gamma_{\rm max}^2$ and $\epsilon < 3\epsilon_1/4\gamma_{\rm min}^2$.

1. If $3\epsilon_1/4\gamma_{\rm min}^2 < \epsilon_s\gamma_{\rm max}^2$ then one sets

$$\epsilon_{\rm max} = 3\epsilon_1/4\gamma_{\rm min}^2 \tag{B.4}$$
$$\epsilon_{\rm min} = \epsilon_s\gamma_{\rm min}^2. \tag{B.5}$$

Thus,

$$\Sigma = \frac{3\epsilon_1}{4\epsilon_s\gamma_{\rm min}^4}, \quad \frac{4}{3}\epsilon_s\gamma_{\rm min}^4 < \epsilon_1 < \frac{4}{3}\epsilon_s\gamma_{\rm min}^2\gamma_{\rm max}^2 \tag{B.6}$$

2. If $3\epsilon_1/4\gamma_{\rm min}^2 > \epsilon_s\gamma_{\rm max}^2$ then

$$\epsilon_{\rm max} = \epsilon_s\gamma_{\rm max}^2 \tag{B.7}$$

However, synchrotron photons with energy $\epsilon_s\gamma_{\rm min}^2$ cannot be upscattered to energies $\epsilon_1 > \frac{4}{3}\epsilon_s\gamma_{\rm min}^2\gamma_{\rm max}^2$. In this case the effective minimum energy of the synchrotron photons is given by

$$\epsilon_{\rm min} = \frac{3\epsilon_1}{4\gamma_{\rm max}^2} \tag{B.8}$$

Thus we find

$$\Sigma = \frac{4\epsilon_s\gamma_{\rm max}^4}{3\epsilon_1}, \quad \frac{4}{3}\epsilon_s\gamma_{\rm min}^2\gamma_{\rm max}^2 < \epsilon_1 < \frac{4}{3}\epsilon_s\gamma_{\rm max}^4 \tag{B.9}$$

Summarizing,

$$\epsilon_1 J_{\rm ic} \propto \epsilon_1^{-\frac{(p-3)}{2}} \begin{cases} \ln\left(\frac{3\epsilon_1}{4\epsilon_s\gamma_{\rm min}^4}\right), & \frac{4}{3}\epsilon_s\gamma_{\rm min}^4 < \epsilon_1 < \frac{4}{3}\epsilon_s\gamma_{\rm min}^2\gamma_{\rm max}^2 \\ \ln\left(\frac{4\epsilon_s\gamma_{\rm max}^4}{3\epsilon_1}\right), & \frac{4}{3}\epsilon_s\gamma_{\rm min}^2\gamma_{\rm max}^2 < \epsilon_1 < \frac{4}{3}\epsilon_s\gamma_{\rm max}^4 \end{cases} \tag{B.10}$$

The function above has a peak at the characteristic energy

$$\epsilon_{\rm peak} = \frac{4}{3}\epsilon_s\gamma_{\rm min}^2\gamma_{\rm max}^2 \tag{B.11}$$

References

Barthelmy, S. D., Cannizzo, J. K., Gehrels, N., et al. 2005, ApJ, 635, L133
Blandford, R. D. & McKee, C. F. 1976, Physics of Fluids, 19, 1130
Blumenthal, G. R. & Gould, R. J. 1970, Reviews of Modern Physics, 42, 237
Butler, N. R. & Kocevski, D. 2007, ApJ, 668, 400
Dermer, C. D. 2007, ApJ, 664, 384
Dermer, C. D., Böttcher, M., & Chiang, J. 2000, ApJ, 537, 255
Dermer, C. D. & Chiang, J. 1998, New Astronomy, 3, 157
Eichler, D. & Granot, J. 2006, ApJ, 641, L5
Evans, P. A., Beardmore, A. P., Page, K. L., et al. 2009, MNRAS, 397, 1177
Evans, P. A., Willingale, R., Osborne, J. P., et al. 2010, A&A, 519, A102+
Fan, Y. & Piran, T. 2006, MNRAS, 369, 197
Fan, Y., Piran, T., Narayan, R., & Wei, D. 2008, MNRAS, 384, 1483
Fenimore, E. E., Epstein, R. I., & Ho, C. 1993, A&AS, 97, 59
Ghisellini, G. 2008, in American Institute of Physics Conference Series, Vol. 1000, American Institute of Physics Conference Series, ed. M. Galassi, D. Palmer, & E. Fenimore, 448–451
Ghisellini, G., Ghirlanda, G., Nava, L., & Firmani, C. 2007, ApJ, 658, L75
Giannios, D. & Spitkovsky, A. 2009, MNRAS, 400, 330
Gould, R. J. 1979, A&A, 76, 306
Granot, J., Königl, A., & Piran, T. 2006, MNRAS, 370, 1946
Granot, J. & Kumar, P. 2006, MNRAS, 366, L13
Granot, J. & Sari, R. 2002, ApJ, 568, 820
Liang, E., Zhang, B., & Zhang, B. 2007, ApJ, 670, 565
Lithwick, Y. & Sari, R. 2001, ApJ, 555, 540
Mastichiadis, A. & Kazanas, D. 2009, ApJ, 694, L54
Mastichiadis, A. & Kirk, J. G. 1995, A&A, 295, 613
Mészáros, P. & Rees, M. J. 1997, ApJ, 476, 232
Nousek, J. A., Kouveliotou, C., Grupe, D., et al. 2006, ApJ, 642, 389
Paczynski, B. & Rhoads, J. E. 1993, ApJ, 418, L5+
Panaitescu, A. & Kumar, P. 2000, ApJ, 543, 66
Panaitescu, A. & Mészáros, P. 1998, ApJ, 501, 772
Panaitescu, A., Mészáros, P., Burrows, D., et al. 2006, MNRAS, 369, 2059
Pe'er, A. & Waxman, E. 2004, ApJ, 613, 448
Petropoulou, M. & Mastichiadis, A. 2009, A&A, 507, 599
Piran, T. 1999, Phys. Rep., 314, 575
Piran, T. 2004, Reviews of Modern Physics, 76, 1143
Press, W. H., Teukolsky, S. A., Vetterling, W. T., & Flannery, B. P. 1992, Numerical recipes in FORTRAN. The art of scientific computing, ed. Press, W. H., Teukolsky, S. A., Vetterling, W. T., & Flannery, B. P.
Rees, M. J. & Mészáros, P. 1992, MNRAS, 258, 41P
Sari, R. & Esin, A. A. 2001, ApJ, 548, 787
Sari, R., Piran, T., & Narayan, R. 1998, ApJ, 497, L17+
Schady, P., Mason, K. O., Page, M. J., et al. 2007, MNRAS, 377, 273
Shao, L., Dai, Z. G., & Mirabal, N. 2008, ApJ, 675, 507
Sironi, L. & Spitkovsky, A. 2009, ApJ, 707, L92
Spitkovsky, A. 2008, ApJ, 682, L5
Tagliaferri, G., Goad, M., Chincarini, G., et al. 2005, Nature, 436, 985
Vaughan, S., Goad, M. R., Beardmore, A. P., et al. 2006, ApJ, 638, 920
Wijers, R. A. M. J. & Galama, T. J. 1999, ApJ, 523, 177
Zhang, B., Fan, Y. Z., Dyks, J., et al. 2006, ApJ, 642, 354
Zhang, B., Liang, E., & Zhang, B. 2007, ApJ, 666, 1002